IEEE Access
Multidisciplinary | Rapid Review | Open Access Journal

Received June 13, 2019, accepted August 6, 2019, date of publication August 12, 2019, date of current version August 30, 2019.

Digital Object Identifier 10.1109/ACCESS.2019.2934418

Reliable Through-Metal Wireless Communication Using Magnetic Induction

HONGZHI GUO, (Member, IEEE), AND KYO D. SONG
Engineering Department, Norfolk State University, Norfolk, VA 23504, USA
Corresponding author: Hongzhi Guo (hguo@nsu.edu)

ABSTRACT Wireless sensors or robots in metal-constrained environments leverage through-metal wireless communications to send data and receive instructions. It is well-known that wireless radio frequency (RF) signals cannot penetrate through metal efficiently, which prevents us from applying existing wireless solutions. Moreover, most applications, e.g., metal inspection robots in an oil pipeline, require noncontact wireless communications, where the ultrasonic signals do not work. To this end, we propose to use magnetic induction communication to provide a reliable and flexible solution for wireless sensor and robotic networks in metal-constrained environments. We consider the transceivers are located on two different sides of a metal wall. Then, we develop an analytical model to obtain the optimal configurations of the magnetic coil and the carrier frequency to maximize the communication channel capacity. The received power and wireless channel bandwidth are studied. The results show that the optimal carrier frequency is around 1 kHz. In addition, we study the negative effects caused by coil misalignment and interference, which are circumvented by leveraging a coil array with optimal receiving strategy. The results are evaluated using numerical simulation and verified by finite element method-based simulation.

INDEX TERMS Coil array, extreme environments, magnetic induction, optimal frequency, through-metal wireless communications.

I. INTRODUCTION

Metal is extensively used to make containers of hazardous materials, oil/gas transportation pipelines, spacecrafts, submarines, among others. Recently, the evolve of wireless sensor and robotic networks provide a convenient way to monitor the environment inside metal structures. For example, sensors are deployed inside of metal tanks to report real-time information about tank pressure, fluid level and temperature [2]; intelligent robots can travel in metal pipes to detect metal corrosion [3]–[5]; and wireless sensors can monitor environmental and mechanical status outside of submarines or ships [6].

Although the metal wall provides impermeable environments, it also prevents us from communicating with sensors or robots that are deployed on the other side due to the following two reasons. First, existing wired communication technologies are not suitable since the deployment of wires can destroy the mechanical strength of the metal and cause leakage. A submarine has to use up to 300 penetrations of the hull to wire the communication cables for sensors outside of it [6]. Second, wireless technologies using UHF or mmWave signals cannot penetrate through metal walls since the skin depth is small and the power absorption is large. As a result, through-metal communication has been a long standing challenging problem.

Different from electromagnetic (EM) waves, the acoustic signals use mechanical vibration to transmit signals, which does not suffer from the high absorption. Acoustic signals have been used to wirelessly transmit information and energy through metal walls. The achievable data rate is on the order of several hundred Mbps and the wireless power transfer efficiency is very high [7], [8]. While the performance is promising, it relies on direct contact with metal surface to create significant vibrations and the transmitter and receiver have to be well aligned. This works for sensors with fixed positions, but it does not work well for robots, e.g., mobile inspection robots in pipelines cannot always touch the metal surface with high precision to align with the transceiver on the other side.

In such a scenario, the low frequency Magnetic Induction Communication (MIC) is a more practical solution. As the

The associate editor coordinating the review of this article and approving it for publication was Bora Onat.

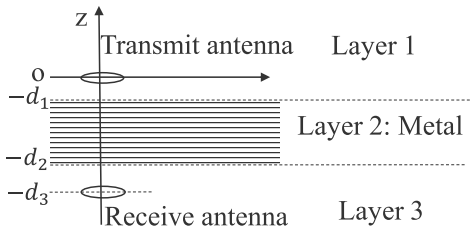

FIGURE 1. System coordinates: A metal wall with thickness $d_2 - d_1$ is placed in-between of a pair of magnetic transceivers.

carrier frequency reduces, the skin depth becomes large and the signal has better penetration efficiency [9]. This technology has been adopted in through-metal wireless power transfer and communications for more than one decade [9]–[13]. The achievable data rate and wireless power transfer efficiency are much lower than that of acoustic waves, but it does not rely on contact with metal surface, which is more flexible for mobile robots. However, existing works are mainly based on experiments and there is a lack of analytical model to provide more insightful understanding of the magnetic field propagation through metal walls. In these experiments, the carrier frequency varies from 50 Hz to several MHz and the coil profile are also very different [6], [14]. It is not clear what is the optimal configuration, i.e., carrier frequency, coil number of turns, coil size, and coil position. Moreover, the design of wireless sensor or robotic networks relies heavily on an accurate analytical channel model to optimally deploy, localize, and cluster the sensors and robots. Therefore, to enable a large scale network for through-metal applications, an analytical model is desirable.

To this end, we develop an analytical model for through-metal wireless communication using magnetic induction. We consider the transceivers are placed on two different sides of an infinitely large metal wall, as shown in Fig. 1. We first formulate the exact field propagation model without any assumptions. Then, by considering the transceivers are coaxial, we simplify the integral of Bessel functions and derive a closed-form analytical model, which is verified by finite element simulations. By leveraging this model, we maximize the communication channel capacity and study the impacts of metal thickness, optimal coil configurations, and the optimal carrier frequency. After that, we relax the assumption by studying randomly located and orientated receivers. Although the performance reduces dramatically for single-coil transceivers, we propose an approach by using coil-array to make the system reliable and efficient. The optimal receiving algorithm is developed and evaluated.

The rest of this paper is organized as follows. In Section II, the related works are reviewed. In Section III, the exact and simplified channel models for single-coil magnetic induction communication (MIC) are developed and evaluated. The achievable data rate and the limitations of this method are discussed. After that, in Section IV, the approach using coil-array is presented and the optimal receiving algorithm is developed. Finally, this paper is concluded in Section V.

II. RELATED WORKS

The EM shielding using metal has been a popular and effective solution since early 20 century [15]. EM waves can hardly penetrate through metal walls and, thus, through-metal wireless communication is a challenging problem. Recently, there are several attempts using acoustic waves to penetrate through metal walls to provide high-speed wireless communication and high-efficiency wireless power transfer [7], [8], [16]–[19]. Different from EM waves, the acoustics signals are carried by mechanical vibrations, which are not affected by metal's high conductivity. In [16], a prototype is designed to prove the feasibility, which can achieve around 500 bps data rate. Later on, the performance is significantly improved by using OFDM [7], echo cancellation [17], and MIMO-OFDM [8]. As reported in [8], the data rate can be several hundreds of Mbps with around 45 dB signal-to-noise ratio (SNR) and 4 cm thick metal wall. More impressively, the acoustic signal can provide high-efficiency wireless power transfer [7], [18].

However, the acoustic transducer relies on contact with the metal surface to create strong vibrations, which is not always possible. For static wireless sensors this can be achieved easily, but for mobile robots, this requires significant coordination between the robot and outside receiver.

Although it's challenging, explorations of using EM signals to penetrate through metal walls have never stopped. In [10], about 20 kbps data rate can be obtained by using 20 dB SNR at 49 kHz with 2 mm thick metal wall. Moreover, wireless power transfer is designed using 50 Hz carrier frequency to reduce the propagation loss. Similar results were also reported in [2], [12]. In these works, the frequency is selected by doing experiments and there is no guideline on the optimal frequency. More recently, [13] presents experimental results, which show that the optimal frequency for magnetic induction-based through-metal wireless power transfer is around 500 to 1000 Hz. Readers are referred to [6], [11] for a more complete review.

The magnetic induction-based solution does not rely on contact with the metal surface, which is desirable for mobile robots. Also, the transceivers can be slightly misaligned without losing connectivity. Thus, it is a promising solution for robots that are moving in metal-constrained environments. Although the optimal frequency based on experiments is reported in [13], there is a lack of analytical model to provide more insightful understanding, which is one of the motivations of this paper. The developed model can also advance our knowledge in many other domains, such as concrete wall monitoring [20].

III. ANALYTICAL MODEL FOR SINGLE-COIL MIC

In this section, we analytically derive a field propagation model and find the key parameters that affect the propagation loss. The system configuration is shown in Fig. 1. A pair of magnetic transceivers are placed coaxially with a metal wall of thickness $d_2 - d_1$ in the middle. The distance between metal wall and transmitting coil is d_1. Usually, a robot or sensor is

much smaller than metal wall. Thus, we can safely consider the metal wall is flat and infinitely large.

A. EXACT MODEL

When an active coil antenna is placed close to a metal wall, it induces eddy currents in the high-conductivity metal. The magnitude of eddy current depends on the excitation current and its frequency. The eddy current re-radiates fields into space, which can create destructive effects [21], [22]. In this paper, we use a general layered model. According to [23], the magnetic fields above and below the metal walls can be expressed as

$$H_{1z} = \frac{-jIA}{4\pi}\int_0^\infty \frac{k_\rho^3 dk_\rho}{k_{1z}} J_0(k_\rho\rho)\left[e^{jk_{1z}|z|} + \tilde{R}_{12}e^{jk_{1z}(z+2d_1)}\right] \tag{1}$$

$$H_{3z} = \frac{-jIA}{4\pi}\int_0^\infty \frac{k_\rho^3}{k_{3z}} J_0(k_\rho\rho)\tilde{T}_{13}e^{jk_{3z}|z|}dk_\rho, \tag{2}$$

where I and $A = n_c\pi a^2$ are the current and overall area of the transmit coil antenna, respectively; n_c is the number of turns, a is the coil radius, k_i is the propagation constant, $k_i = \sqrt{k_\rho^2 + k_{iz}^2} = \omega\sqrt{\mu_i\epsilon_i}$, ω is the angular frequency, μ_i is the permeability, ϵ_i is the complex permittivity, $J_0(x)$ is the zero order Bessel function of the first kind, ρ is the horizontal distance, $\tilde{R}_{12}$ is the reflection coefficient of the boundary between layer 1 and 2 considering the existence of layer 3, and $\tilde{T}_{13}$ is the transmission coefficient through the metal layer. H_{3z} is a key parameter to derive the mutual inductance between the transmitter and receiver, which determines the received power. Note that, in (1) and (2), the integrable variable is k_ρ, which is from 0 to ∞.

When a coil is vertically orientated, it generates TE wave and the corresponding reflection and transmission coefficients are

$$R_{ab} = \frac{\mu_b k_{az} - \mu_a k_{bz}}{\mu_b k_{az} + \mu_a k_{bz}};$$
$$T_{ab} = \frac{2\mu_b k_{az}}{\mu_b k_{az} + \mu_a k_{bz}}, \tag{3}$$

where $|a - b| = 1$, and R_{ab} and T_{ab} are the reflection and transmission coefficients between layer a and b, respectively.

Following the method in [23, chap. 2], we can find

$$\tilde{R}_{12} = R_{12} + \frac{T_{12}R_{23}T_{21}e^{2jk_{2z}(d_2-d_1)}}{1 - R_{23}R_{21}e^{j2k_{2z}(d_2-d_1)}}$$
$$\tilde{T}_{13} = \frac{T_{12}T_{23}e^{jk_{2z}(d_2-d_1)}}{1 - R_{23}R_{21}e^{j2k_{2z}(d_2-d_1)}}. \tag{4}$$

Observe that (2) has exponential functions and Bessel functions, and (4) are functions of k_{rho}, which makes the integral more complicated. Therefore, it is a great challenge to efficiently compute and obtain insightful results. Next, we try to derive a closed-form solution to solve (2).

B. ANALYTICAL APPROXIMATIONS

In the following, we use asymptotic approximations of high frequency and low frequency to simplify the model. Note that, different from traditional definitions, here the high frequency and low frequency are defined based on the skin depth.

1) HIGH FREQUENCY APPROXIMATION - PENETRATED MAGNETIC FIELD

Since the transceivers are placed coaxially, ρ is 0 in (2), upon which we can simplify the Bessel function, i.e., $J_0(k_\rho\rho) = 1$. Also, when carrier frequency is high, only if k_ρ is in the range $k_1 < k_\rho < |k_2|$, it can make significant contributions to the integral. Thus, we can assume that $k_{1z} = k_{3z} \approx jk_\rho$ and $k_{2z} \approx k_2$. Next, by using (3) we approximately obtain

$$T_{12}\cdot T_{23} \approx \frac{2j}{j + \frac{k_2}{k_\rho}}\cdot\frac{2k_2}{k_2 + k_\rho j} \approx \frac{4k_2k_\rho j}{2k_2k_\rho j + k_2^2}. \tag{5}$$

Similarly, we can find

$$R_{21}\cdot R_{23} \approx \frac{k_2 - k_\rho j}{k_2 + k_\rho j}\cdot\frac{k_2 - k_\rho j}{k_2 + k_\rho j} \approx \frac{k_2^2 - 2k_2k_\rho j}{k_2^2 + 2k_2k_\rho j}. \tag{6}$$

Finally, $\tilde{T}_{13}$ can be approximated by

$$\tilde{T}_{13} \approx \frac{4jk_2k_\rho e^{jk_2(d_2-d_1)}}{k_2^2 + 2jk_2k_\rho - (k_2^2 - 2jk_2k_\rho)e^{2jk_2(d_2-d_1)}}. \tag{7}$$

Then, using (7) we can obtain the simplified (2), which is

$$H_{3z} \approx -\frac{jIA}{\pi}e^{jk_2(d_2-d_1)}\int_0^\infty \frac{k_\rho^3 e^{-k_\rho|z|}}{\xi_1 + k_\rho\xi_2}dk_\rho \tag{8}$$

$$\approx -\frac{jIA}{\pi}e^{jk_2(d_2-d_1)}\int_{k_1}^{\xi_3} \frac{k_\rho^3 e^{-k_\rho|z|}}{\xi_1 + k_\rho\xi_2}dk_\rho \tag{9}$$

where $\xi_1 = k_2 - k_2e^{2jk_2(d_2-d_1)}$, $\xi_2 = 2j[1 + e^{2jk_2(d_2-d_1)}]$, and $\xi_3 = \sqrt{\pi f\mu_0\sigma}$. Note that, ξ_1 and ξ_2 are not functions of k_ρ. To find a closed-form solution to (8), we use the following approximations.

- The integrand is dominant only if $k_1 < k_\rho < |k_2|$. Therefore, we can approximate (8) using (9). Here, k_ρ is integrated along the real axis, but k_2 is a complex number, which can be approximated by $k_2 \approx \xi_3 + j\xi_3$ since the metal is a good conductor. Also, note that the real part and the imaginary part of k_2 are the same. If we integrate from k_1 to k_2 it changes the original path. To avoid this issue, we only take the real part of k_2.
- Since $e^{2jk_2(d_2-d_1)}$ denotes the propagation of magnetic fields in the metal, it is small due to the lossy medium. As a result, we can obtain $\xi_1 \approx k_2$ and $\xi_2 \approx 2j$.
- In addition, $\xi_1 + k_\rho\xi_2$ can be further approximated by k_2 because $k_\rho < |k_2|$.

Using the above approximates, (9) can be simplified to

$$H_{3z} \approx -\frac{jIA}{k_2\pi}e^{jk_2(d_2-d_1)}\int_{k_1}^{\xi_3} k_\rho^3 e^{-k_\rho|z|}dk_\rho. \tag{10}$$

The integral in (10) can be solved in the following way:

$$\int_{k_1}^{\xi_3} k_\rho^3 e^{-k_\rho|z|} dk_\rho = -\frac{\left(|z|^3x^3 + 3|z|^2x^2 + 6|z|x + 6\right)e^{-|z|x}}{|z|^4}\Big|_{k_1}^{\xi_3}$$
$$\approx \frac{6}{|z|^4}. \quad (11)$$

The value of ξ_3 is large and thus the exponential function $e^{-|z|\xi_3}$ is negligible. On the contrary, since k_1 is small, we have $e^{-|z|k_1} \approx 1$ and the dominant term in the parenthesis is 6. As a result, we can obtain the simplified solution in (11). By substituting (11) to (10) and express k_2 using ξ_3, we have

$$H_{3z} = \frac{6IAe^{j\sqrt{\pi f\sigma\mu_0}(d_2-d_1)}}{(-1+j)\pi\sqrt{\pi\sigma\mu_0}|z|^4} f^{-\frac{1}{2}} e^{-\sqrt{\pi f\sigma\mu_0}(d_2-d_1)}. \quad (12)$$

Also, to illustrate the physics better, we can obtain the absolute value of the penetrated magnetic field using natural logarithm

$$\log(|H_{3z}|) = \log(6IA) - \log(\pi\sqrt{2\pi\sigma\mu_0}) - 4\log(|z|) - \frac{1}{2}\log f - \sqrt{\pi f\sigma\mu_0}(d_2 - d_1). \quad (13)$$

In view of (13), the magnetic field magnitude is monotonically decreasing with the carrier frequency, conductivity, and the metal thickness. The last term on the right-hand side of (13) can be rewritten as $(d_2 - d_1)/\delta$, where $\delta = 1/\sqrt{\pi f\sigma\mu_0}$ is the skin depth. This can be regarded as the loss of a plane wave propagating in the metal. Therefore, (13) is a comprehensive model that considers both the near-field effect the far-field plane wave approximations.

2) HIGH FREQUENCY APPROXIMATION - REFLECTED MAGNETIC FIELD

Similar as the $\tilde{T}_{13}$, we can use the high-frequency approximations, i.e., $k_{1z} = jk_\rho$ and $k_{2z} = k_2$, to derive the simplified $\tilde{R}_{12}$, which is

$$\tilde{R}_{12} \approx -1 + \frac{4jk_2k_\rho(k_2 - jk_\rho)e^{2jk_2(d_2-d_1)}}{(k_2 + jk_\rho)^3 - \xi_4 e^{2jk_2(d_2-d_1)}}, \quad (14)$$

where $\xi_4 = (k_2 - jk_\rho)^2(k_2 + jk_\rho)$ and we implicitly use $\frac{jk_\rho - k_2}{jk_\rho + k_2} \approx -1$ since $k_\rho < |k_2|$. Also, the exponential function in (14) is nearly 0 and, thus, the second term on the right-hand side of (14) can be neglected. As a result, $\tilde{R}_{12} \approx -1$. This result is consistent with traditional understanding that metal is hard to penetrate and most of the fields are reflected.

The reflected field can change the coil property, such as impedance. This is leveraged to detect metals in complex environments. By considering $\tilde{R}_{12} \approx -1$, we have

$$H_{1z} = \frac{-IA}{4\pi}\left[\int_0^\infty k_\rho^2 e^{-k_\rho|z|}dk_\rho - \int_0^\infty k_\rho^2 e^{-k_\rho(z+2d_1)}dk_\rho\right]$$
$$\approx \frac{IA}{2\pi}\left[\frac{1}{(z+2d_1)^3} - \frac{1}{|z|^3}\right], \quad (15)$$

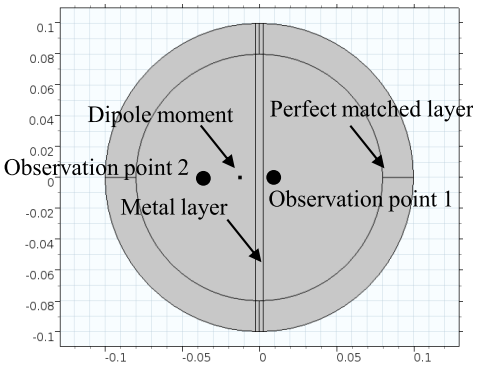

FIGURE 2. Simulation model, size unit: meter.

where the approximation is based on the same method in (10) and (11). Note that, the negative sign denotes the magnetic field direction, which is negative z-direction. The value of H_{1z} is always negative since the reflected field cannot be larger than the incident field. In addition, when d_1 is small, the overall field in layer 1 becomes negligible since there is a virtual image of the coil in the metal which cancels the fields that are generated by the original coil.

3) LOW FREQUENCY APPROXIMATION

Note that when the frequency is extremely low, k_2 becomes comparable with k_1 and the integrand in (2) spreads across a wide range of k_ρ. As a result, k_ρ can be much larger than k_2 and we can obtain the following approximations: $k_{1z} = k_{2z} = k_{3z} = ik_\rho$. In this way, we can consider the layer 1, 2, and 3 have the same propagation constant, and thus $\tilde{T}_{13} \approx 1$ and $\tilde{R}_{12} = 0$. Intuitively, when the frequency is extremely low, the metal layer is transparent due to the large skin depth and, thus, the transmission coefficient is 1. Under this assumption, the transmitted magnetic field is

$$H_{3z} = \frac{-IA}{4\pi}\int_0^\infty k_\rho^2 e^{-k_\rho|z|}dk_\rho \approx -\frac{IA}{2\pi|z|^3}. \quad (16)$$

In view of (16), when the frequency is extremely low, the magnetic field penetrated through the metal is independent of frequency. Also, the field in layer 1 can be characterized by using (16) since the metal layer is transparent to the magnetic fields in the low-frequency regime.

4) NUMERICAL SIMULATION AND ANALYSIS

Next, we conduct numerical simulations and compare the results with the developed analytical models. The geometric model built in COMSOL Multiphysics is shown in Fig. 2. A 3D illustration of the simulation model is shown in Fig. 3. The outer layer of the simulation space is a perfect matched layer to avoid boundary reflections. To simulate the infinite large metal wall, we extend the metal to the perfect matched layer. The magnetic coil is simulated by a dipole moment, which is 1 cm away from the metal wall and its orientation is perpendicular to the metal wall. The considered metal is aluminum and its conductivity is 3.774×10^7 S/m. In the

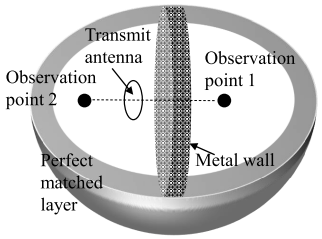

FIGURE 3. 3D illustration of the simulation model.

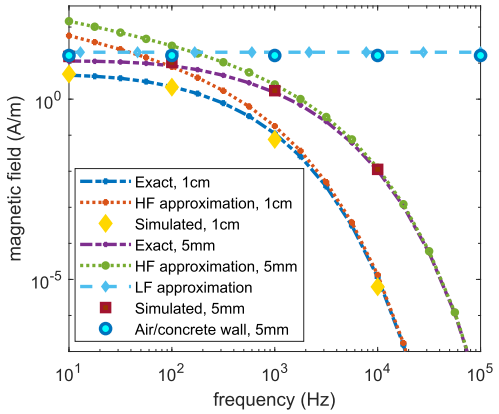

FIGURE 4. Penetrated magnetic field intensity (the observation point 1 is on the right side of the metal wall with distance 1 cm).

simulation, to determine the dipole moment, we create a real coil with radius 2.5 cm and 1 A excitation current. Then, we measure its radiated magnetic field and scale the dipole moment to generate the same magnetic field, which is 0.066 m^2·A. We consider two different metal thickness, i.e., 1 cm and 5 mm to show the effect of metal thickness. In the analytical model, we consider the wire is made of copper with conductivity 5.96×10^7 S/m and 0.5 mm in radius. The radius of the wire is small in order to reduce coil weight and its occupied space. Also, the analytical model in (2) assumes that the coil is an infinitesimal dipole which has negligible radius.

The penetrated magnetic field intensity at observation point 1 (1 cm away from the metal wall) is shown in Fig. 4. When carrier frequency is smaller than 200 Hz, the magnetic field intensity does not change as frequency increases. When carrier frequency is larger than 200 Hz, magnetic field intensity decreases dramatically. Moreover, magnetic fields experience more attenuation when metal thickness is larger. Both high-frequency approximation and low-frequency approximation can capture the trend of field attenuation well. Also, to show the effect of the metal wall better, we consider a virtual air wall and a concrete wall with thickness of 5 mm. The simulated results suggest that when carrier frequency is lower than 100 kHz, signals can easily penetrate through the air and concrete without absorption loss or reflection loss. This is mainly due to the long wavelength and skin depth.

The overall magnetic field intensity in layer 1 is shown in Fig. 5. The magnetic field is measured at observation point 2 which is 2.5 cm (coil radius) left of the coil center.

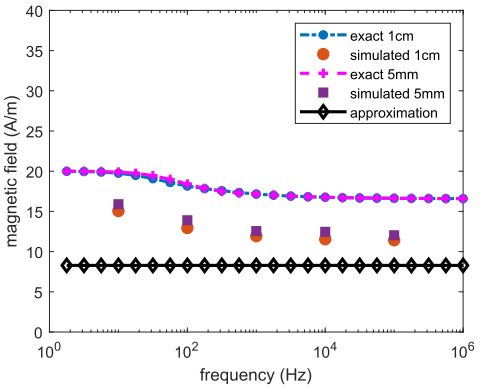

FIGURE 5. Overall magnetic field intensity in layer 1 (the observation point 2 is 2.5 cm left of the transmit coil center).

In this way, we can avoid the singularity of the approximation in (15). The approximation suggests that the intensity does not change with frequency. As shown in the figure, both the simulated and exact results show that the magnetic field intensity decreases slightly as carrier frequency increases. However, the change is negligible, i.e., the field can be approximated by a constant value. In addition, there is around 3 dB difference between the approximated value and the exact solution, which is negligible compared to the several tens of dB field attenuation. The computation error comes from numerical integral and simplifications.

In Fig. 6, the magnetic field intensity is shown visually. To display the field intensity better, we scale the field by using the function $\log_{10}(h)$. At 100 Hz, the field can penetrate through the metal wall well, while as frequency increases to 1 kHz, the penetrated field becomes weaker. Further increasing the frequency to 10 kHz, there is almost no penetrated magnetic field. Note that, here we create an infinitely large metal wall to avoid field leakage from the boundary. The finite-size metal wall problem is investigated in [24]. Although magnetic fields with low frequency can penetrate through the metal wall more efficiently, it does not mean that it is better to use low frequency signals because strong magnetic coupling requires high carrier frequency. Therefore, there is a trade-off between efficiency and coupling. To study this problem, we first investigate the effect of metal on coils and, then, we apply the equivalent circuit model to find the optimal frequency.

C. EFFECT OF METAL WALL ON COILS

It is well-known that the proximity to conductive materials can significantly change antenna's property, including radiation pattern and impedance. The equivalent circuit model for MIC can jointly characterize the wireless channel and coil impedance [25]. Two of the key parameters that are affected by metal are the mutual inductance and self-inductance, which have impacts on communication bandwidth and the coupling between transmitter and receiver. Next, by using the analytical model, we examine the change of mutual inductance and self-inductance. The negative sign in the magnetic

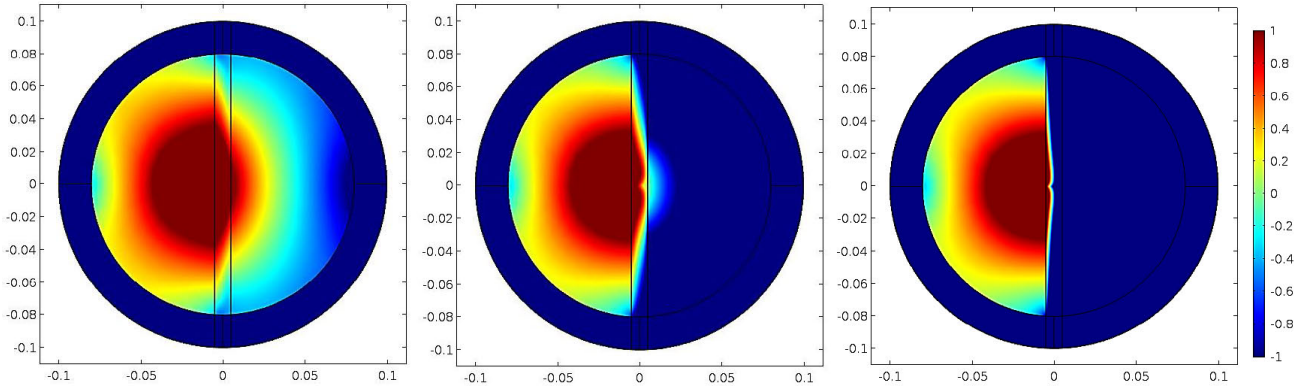

(a) 100 Hz (b) 1 kHz (c) 10 kHz

FIGURE 6. Magnetic field intensity with carrier frequency 100 Hz, 1 kHz, and 10 kHz. The magnetic field (h) is displayed by using $\log_{10}(h)$.

fields denotes negative z-direction. When we calculate the inductance, this negative sign is neglected since inductance does not have a direction.

1) MUTUAL INDUCTANCE

The mutual inductance is the ratio of the magnetic flux linkage over the excitation current. Since the receiving coil is small, we assume the magnetic flux going through the coil is uniform. Then, we can obtain the mutual inductance under the high-frequency approximation, which is [26]

$$M_{high} = -\frac{6A^2\sqrt{\mu_0}e^{j\sqrt{\pi f\sigma\mu_0}(d_2-d_1)}}{(j-1)\pi\sqrt{\pi\sigma}|z|^4}f^{-\frac{1}{2}}e^{-\sqrt{\pi f\sigma\mu_0}(d_2-d_1)}, \tag{17}$$

and the mutual inductance under the low-frequency approximation is

$$M_{low} = \frac{\mu_0 A^2}{2\pi|z|^3}. \tag{18}$$

Note that, M_{high} is a complex number and M_{low} is purely real. The reason is that magnetic fields experience significant phase shift in the metal wall due to the short wavelength (the high conductivity significantly reduces the wavelength), while in the low-frequency regime, the phase shift is negligible because of the long skin depth.

2) SELF-INDUCTANCE

The self-inductance is affected by the reflected fields. By using (15), we can obtain the self-inductance with the high-frequency approximation, which is

$$L = \frac{\mu_0 A^2}{2\pi}\left[-\frac{1}{(a+2d_1)^3}+\frac{1}{a^3}\right] \approx \frac{\mu_0 n_c^2 \pi a}{2}. \tag{19}$$

The approximation in the above equation is based on the observation that d_1 is comparable to a and the first term in the bracket can be neglected, i.e., we do not require the transmitter having contact with the metal wall. For the low-frequency approximation, since the reflected fields is almost zero, the self-inductance is not affected by the metal, which is

$$L \approx \frac{\mu_0 n_c^2 \pi a}{2}. \tag{20}$$

When d_1 is not vanishing, the self-inductances are almost the same for the two scenarios because magnetic fields fall-off quickly when frequency is high and, thus, the reflected field travels longer distance, which can be neglected compared with the field generated by the coil. The well-known self-inductance formula for a single-turn coil can be used to compare with the developed model, which is written as [27]

$$L_{exact} = \mu_0 a\left[\log\left(\frac{8a}{r_w}\right)-2\right], \tag{21}$$

where r_w is the wire radius.

The comparisons among the analytical model in (19) and (20), the exact model in (21), and the simulated model are shown in Fig. 7, where a single-turn coil with 2.5 cm in radius is considered. As suggested in the figure, the self-inductance is not a function of carrier frequency, which verifies our previous claim. Since we approximate the magnetic field across the coil by assuming $z = a$, which underestimate the overall magnetic flux. Also, the developed model can match well with the simulated results.

Moreover, the coil AC resistance is [27]

$$R_{ac} = \frac{2n_c a}{\sigma_c\left[r_w^2-\left(r_w-\sqrt{\frac{1}{\sigma_c\pi f\mu_0}}\right)^2\right]}, \tag{22}$$

where σ_c is the conductivity of the wire and r_w is the wire radius. When f is small, only DC resistance is considered, i.e., $R_{dc} = n_c R_0$, where R_0 is the DC resistance of a single turn coil. R_{dc} does not vary with frequency. When carrier frequency is extremely low, R_{ac} can be a negative number, which is not true in reality. Here, we consider the coil resistance is $R_c = R_{ac} + R_{dc}$, only if $R_{ac} > 0$, otherwise, we only consider R_{dc}. When f is large, by expanding the second term in the

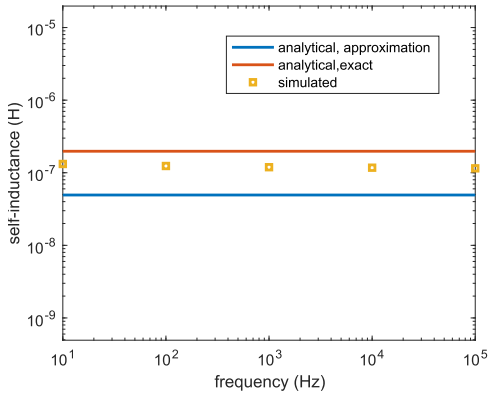

FIGURE 7. Simulated and analytical self-inductance.

denominator, the overall resistance can be approximated by

$$R_c \approx \frac{n_c a}{r_w}\sqrt{\frac{\pi f \mu_0}{\sigma_c}}. \tag{23}$$

The above equation suggests that, the higher the carrier frequency, the larger the AC resistance.

Since the coil bandwidth is determined by the quality factor, which is

$$\begin{aligned} Q(f) &= \frac{2\pi f L}{2R_c} \\ &= \frac{1}{4}\pi^2 n_c \mu_0 \sigma_c f \left[r_w^2 - \left(r_w - \sqrt{\frac{1}{\sigma_c \pi f \mu_0}} \right)^2 \right] \end{aligned} \tag{24}$$

where we implicitly assume the load/source resistance is R_c, i.e., the circuit is matched. Also, the self-inductance is calculated by assuming $z = a$. The bandwidth can be approximated by $B = f_0/Q(f_0)$, where f_0 is the carrier frequency. Under high-frequency assumption, the bandwidth can be written as

$$B = \frac{2}{n_c \pi^2 r_w}\sqrt{\frac{f_0 \pi}{\mu_0 \sigma_c}}. \tag{25}$$

In view of (25), the higher the carrier frequency, the broader the bandwidth.

D. OPTIMAL CONFIGURATIONS: CARRIER FREQUENCY & COIL

Next, we present the received power model, upon which we obtain the optimal configurations to achieve the maximum data rate. The transmission power in a matched coil is

$$P_t = R_c |I|^2. \tag{26}$$

The received power in the receiver can be written as [28]

$$P_r = \frac{R_c |2\pi f M I|^2}{8R_c^2} = \frac{|\pi f M I|^2}{2R_c}. \tag{27}$$

Therefore, we can obtain the signal loss

$$l = -10\log_{10}\frac{P_r}{P_t} = -10\log_{10}\left(\frac{|\pi f M|^2}{2R_c^2}\right). \tag{28}$$

Note that, the above model has a constraint. If the coil resistance is small, P_r can be larger than P_t, which cannot be true. The constraint is that the coil current has a maximum value, beyond which the circuit cannot support. If there is a given transmission power, significantly reducing the coil resistance increases the coil current. Therefore, reduce R_c cannot increase P_r because P_t has to be reduced to satisfy $|I| \le |I_{max}|$, where $|I_{max}|$ is the magnitude of the maximum current in the circuits.

1) HIGH-FREQUENCY APPROXIMATIONS

By substituting (17) into (28), we can obtain the loss of high-frequency approximation. Also, if the frequency is high enough we can simplify the coil resistance to obtain an updated loss, which is

$$\begin{aligned} l &= -10\log\left[\frac{9n_c^2 a^6 \pi^2 r_w^2 \sigma_c}{\sigma |z|^8} e^{-2\sqrt{\pi f \sigma \mu_0}(d_2 - d_1)}\right] \\ &= -10\log\frac{9n_c^2 a^6 \pi^2 r_w^2 \sigma_c}{\sigma} + 80\log|z| + 20\zeta\log e, \end{aligned} \tag{29}$$

where $\zeta = \sqrt{\pi f \sigma \mu_0}(d_2 - d_1)$.

Intuitively, increasing the carrier frequency can improve the coupling between coils, but it reduces the penetration efficiency. Thus, there is an optimal frequency, i.e., there is a trade-off between penetration efficiency and coil coupling. However, (29) reveals that the loss increases monotonically with frequency since the coupling effect is canceled by the increase of AC resistance. An important observation is that in the high-frequency regime, the penetration loss is dominant, rather than the coupling strength.

The Shannon channel capacity for an AWGN channel can be written as

$$C = B\log_2\left[1 + \frac{P_t l}{N_n B}\right], \tag{30}$$

where N_n is the noise power density. The above equation is also subject to the constraint that $\sqrt{P_t/R_c} \le |I_{max}|$. In most applications, the coil size is another constraint, i.e., $0 < a \le a_{max}$, but (30) suggests that the capacity increases monotonically with a and thus the optimal value of a is a_{max}. The effect of n_c is two-fold. When the received SNR is large, the capacity decreases as the coil number of turns increases since the n_c out of the bracket affects the capacity more than the one in the bracket. On the other hand, when SNR is small, since $log_2(1+SNR) \approx SNRlog_2\, e$ the capacity is proportional to n_c^2. As a result, we need to reduce n_c to increase bandwidth when SNR is large, while we need to increase n_c to increase the received signal strength when SNR is small. Thus, given the carrier frequency, there is an optimal number of turns to maximize the channel capacity.

2) LOW-FREQUENCY APPROXIMATIONS

In the low-frequency regime, the coil resistance and the received signal are independent of the carrier frequency. The AC resistance of the coil can be neglected. The signal loss

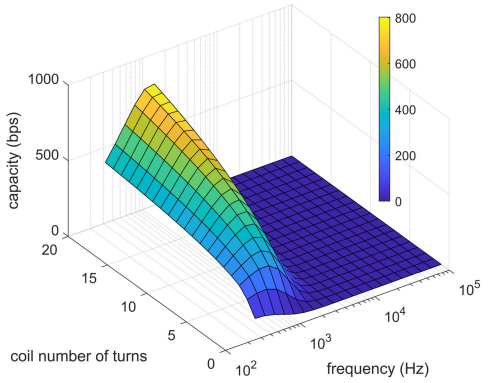

FIGURE 8. Effect of coil number of turns and frequency on channel capacity. Noise level: −90 dBm/Hz.

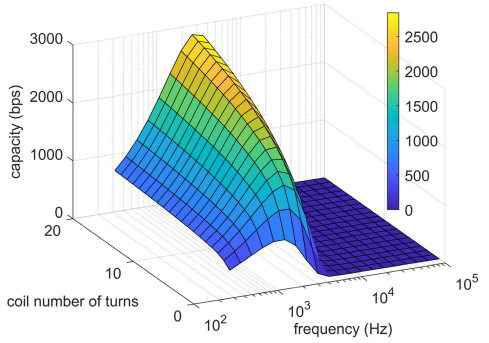

FIGURE 9. Effect of coil number of turns and frequency on channel capacity. Noise level: −120 dBm/Hz.

becomes

$$l = -10\log\left(\frac{f_0^2\mu_0^2 n_c^2\pi^4 a^8}{8R_0^2|z|^6}\right). \tag{31}$$

Different from the high-frequency scenario, the signal loss in low-frequency regime decreases as the carrier frequency increases due to the strong coupling. Using the same method as the high-frequency approximation, we have the approximated bandwidth

$$B = \frac{2R_0}{n_c\mu_0\pi^2 a}. \tag{32}$$

Then, the channel capacity can be written as

$$C = \frac{2R_0}{n_c\mu_0\pi^2 a}\log_2\left[1 + \frac{P_t f_0^2\mu_0^3 n_c^3\pi^6 a^9}{16R_0^3 N_n|z|^6}\right]. \tag{33}$$

In view of (33), the capacity increases monotonically with the carrier frequency. In the low-frequency regime, the optimal capacity is achieved by using the highest frequency. In the low SNR regime, increasing n_c can improve the capacity, while in the high SNR regime, increasing n_c can reduce the capacity due to the narrower bandwidth.

3) NUMERICAL EVALUATION

In Fig. 8 and Fig. 9, the optimal frequency and coil number of turns are shown for the high-frequency approximations with different noise power density. The capacity is computed based on (30), which subjects to the maximum current constraint, maximum area constraint, and the bandwidth constraint. Here, we limit the bandwidth to 10% of the carrier frequency to avoid impractically large bandwidth, i.e., the bandwidth is given by $\min(0.1f_0, B)$. The transmission power is 10 dBm and the maximum current I_{max} is 500 mA. The noise power is −90 dBm/Hz and −120 dBm/Hz, respectively. Also, we notice that it is not accurate to use (23) since the carrier frequency is not high enough. We employ the exact formula in (22).

The results suggest that the optimal frequency for the high noise density is around 1438 Hz, while for the low noise density they are 2637 Hz. The maximum achievable data rate is around 802 bps and 2843 bps for the low noise density and high noise density, respectively. If the frequency is higher than the optimal frequency, the signal strength decreases significantly, while if the frequency is lower than it the bandwidth reduces. When SNR is large, the optimal frequency is high since this can improve the bandwidth. When SNR is small, the optimal frequency is low since this can improve the signal strength.

Also, the more number of turns, the higher the capacity, which is more obvious around the optimal carrier frequency. Since the mutual inductance is proportional to n_c^2 and the coil resistance is proportional to n_c, a large n_c can increase the received power. Although the bandwidth decreases as n_c increases, the capacity is mainly limited by the SNR, instead of bandwidth. For the low-frequency approximation, the capacity increases monotonically with the carrier frequency. Moreover, the bandwidth are broader than $0.1f_0$ and the n_c on the denominator of (33) does not take effect. Therefore, the higher the frequency and n_c, the larger the capacity. Note that, since the carrier frequency is around 1 kHz, while the coil radius is several centimeters, the wavelength is much larger than the coil size. Thus, we can safely consider the coil as an infinitesimal dipole. As pointed out in [27, Chap. 5], when we consider the antenna as an infinitesimal dipole, no matter it is circular or square, the generated fields are the same.

IV. IMPROVE RELIABILITY USING COIL ARRAY

Due to the unpredictable orientation and location, reliability of the system needs to be improved from two aspects. First, the random orientation of the transceiver causes significant loss, which makes the system unreliable. Second, the interference generated by multiple transceivers that are close to each other can dramatically reduce the communication data rate. For example, in a crucial area of a metal wall, there may be several sensors monitoring the status and collecting various data, which can communicate simultaneously. To reduce the interference, we have to limit the maximum number of transceivers or their transmission power. In this section, we first study the orientation and interference issues. Then, we propose to use coil array to improve system reliability.

A. COIL MISALIGNMENT

Recall that in (2) we can simplify it since the coils are coaxial and the Bessel function becomes a constant due to its singularity. Although this makes the problem solvable, in reality it is challenging to align coils co-axially for through-metal communications. Without loss of generality, we consider the transmit coil is parallel to the metal wall and its position is fixed, which is the same as preceding discussions, while the receive coil has arbitrary orientation and position. This assumption is practical since most through-metal applications have a detector/receiver with fixed location and orientation outside of the sealed metal pipe/container and a sensor/robot with random location and orientation inside the metal pipe/container. Also, due to the reciprocity, communication performances do not change if we switch the positions of transmitter and receiver. Additionally, it is easy to make smart devices parallel with the metal surface, but it is hard to infer the position of the other coil on the other side of the metal due to the blockage.

Since the orientation and location of the receiver is arbitrary, we need to derive the magnetic field intensity for the horizontal directions. According to [23], the horizontal magnetic fields can be written as

$$(h_{3\rho}, h_{3\phi}) = \int_0^\infty \frac{1}{k_\rho^2}\left(\frac{\partial}{\partial\rho}\frac{\partial h_{3z}}{\partial z}, \frac{1}{\rho}\frac{\partial}{\partial\phi}\frac{\partial h_{3z}}{\partial z}\right) dk_\rho$$
$$= \frac{IA}{4\pi}\int_0^\infty \left(k_\rho^2 J_1(k_\rho\rho), 0\right) \mathcal{T}_{13} e^{-jk_{3z}z} dk_\rho, \quad (34)$$

where $J_1(k_\rho\rho)$ is the Bessel function with order 1. Now, we consider the magnetic fields in layer 3 is a vector $\boldsymbol{h}^T = [h_\rho, h_\phi, h_z]$, and $\boldsymbol{\Phi} = [\cos\phi, -\sin\phi, 0; \sin\phi, \cos\phi, 0; 0, 0, 1]$ is a matrix which can convert Cylindrical coordinates to Cartesian coordinates. Also, the coil orientation is denoted by a unit vector $\boldsymbol{u} = [u_x, u_y, u_z]$, which is the direction of the coil's axis. The mutual inductance between the transmit coil and the receive coil can be written as

$$M = \frac{A\mu_0 \boldsymbol{u}\cdot\boldsymbol{\Phi}\cdot\boldsymbol{h}}{I}. \quad (35)$$

By substituting (35) into (28) we can obtain the signal loss. Since ρ can be larger than zero, the Bessel function cannot be simplified and, thus, there is no closed-form solution [23]. Therefore, we cannot obtain simple formula to reveal the underlying relations between the optimal performance and coil configurations. Instead, we use numerical simulations to evaluate the reliability. Note that, the coil self-inductance and resistance are almost not affected by the orientation and location, i.e., the bandwidth does not change. Based on this model, we analyze the effect of orientation and location numerically.

In Fig. 10, magnetic field intensity on three horizontal planes are shown. Only one dimension is shown due to the symmetry. The plane is parallel with the metal wall and the distance from the lower surface of the metal wall to each plane

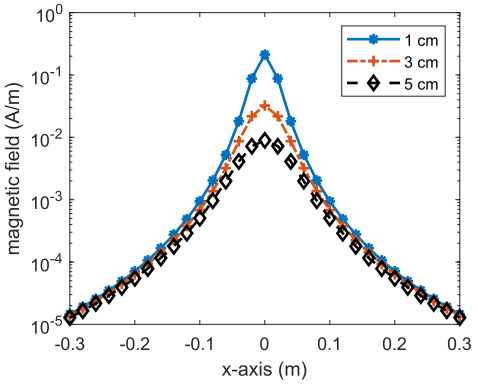

FIGURE 10. Penetrated magnetic field intensity on a horizontal plane: The plane is 1 cm, 3 cm, and 5 cm under the metal wall. The x-axis coordinate of transmit coil's center is 0 m. Only one dimension is shown due to the symmetry.

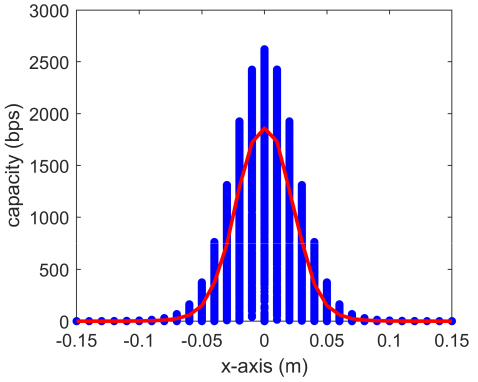

FIGURE 11. Channel capacity with randomly orientated receiving coil. The blue dots are simulated capacity for a receive coil with random orientation. The red curve is the mean value for the random capacity simulated at that location.

is 1 cm, 3 cm, and 5 cm, respectively. We consider a single-turn coil and the carrier frequency is 1900 Hz. The origin (0,0) is right under the transmit coil's center. As we can see from the figure, the magnetic field intensity decreases very fast, i.e., a slightly position deviation may cause significant power loss. Also, as the distance between the metal wall and the receiver increases, and the peak magnetic field reduces dramatically. As a result, to receive strong magnetic field, the receiver has to stay close to the metal wall and be coaxial with the transmitter.

In Fig. 11, we randomly generate the coil orientation by using the approach in [29]. Due to the symmetric property, only the line along x-axis is used here. The capacity is calculated by using 2637 Hz carrier frequency and other parameters are same as previous configurations. As shown in the figure, the capacity is highly random and it has a large variance. Thus, the system cannot provide reliable wireless communications.

B. INTERFERENCE

The results in Fig. 10 and Fig. 11 suggest that after penetrating the metal wall, magnetic fields can propagate for

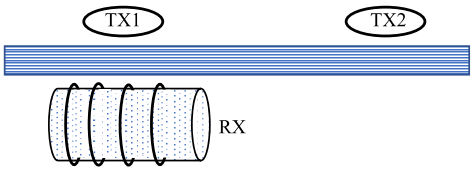

FIGURE 12. Illustration of a receiver with a coil array.

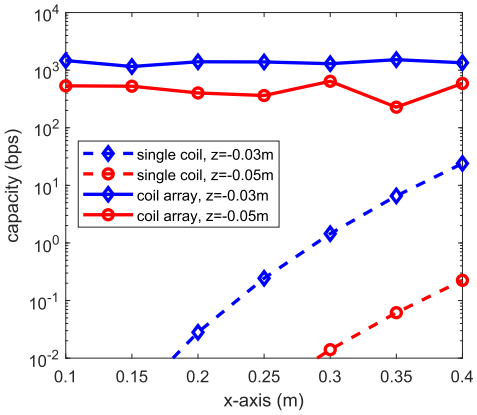

FIGURE 13. The effect of interference by a closely located transmitter. X-axis is the distance between the intended transmitter and the interferer.

a relatively long distance, which can generate interference for other nearby ongoing wireless communications. Next, we try to evaluate the interference effects caused by nearby simultaneous transmitters. We consider the transmitting coil (TX_1) and the receiving coil (RX) are coaxial, which has the same configurations as that in Fig. 10. There is an additional transmitter (TX_2) generating interference and it is on the same plane as the first transmitter, as shown in Fig. 12. TX_2 has the same orientation as TX_1, i.e., vertically orientated. The distance between them is a variable d_t. In this scenario, we consider SINR (signal to interference and noise ratio), where the interference power is treated as noise power. In this way, the channel capacity can be updated by

$$C = B\log_2\left[1+\frac{P_t\pi^2 f_0^2|M_1|^2}{2R_c^2N_n+P_t^2\pi^2 f_0^2|M_2|^2}\right], \quad (36)$$

where M_1 and M_2 are the mutual inductance between two transmitters and the receiver, respectively. The transmission power P_t and resistance R_c are the same for transmitters.

As shown in Fig. 13, the capacity reduced significantly due to the interference. When the receiving coil is 0.04 m away from the lower surface of the metal wall, the data rate reduces to nearly zero. This is mainly due to the following two reasons. First, when $z = -0.03$ m, the receiving coil is close to the transmitting coil, its received power is large. Second, when $z = -0.03$ m, TX_1 is closer to the receiver than TX_2 and thus the interference effect is less severe than that when $z = -0.05$ m. Therefore, to maintain a reliable wireless link, only limited number of transmitters can be placed in a small area. To improve the capacity, we need to explore other diversities. Next, we leverage the coil array to reduce the orientation loss and interference.

C. COIL ARRAY

As shown in Fig. 12, a coil array is employed on a sensor/robot. For a metallic tank or pipe, the outside transmitters inquiring real-time data from the sensor/robot. Due to the reciprocity, the transmitter and receiver can switch positions, without changing the communication performance. The coil array can be arranged on a plane [30] or a cylinder [31]. We adopt the second approach since it is easy to be accommodated on a robot.

We consider there are N_c elements in the coil array, i.e., $r_1, r_2, \cdots, r_{N_c}$, and all the elements have the same configuration as the receiving coil in preceding discussions. Then, according to Kirchhoff's Voltage Law, the coil array current induced by the two transmitting coils can be written as

$$\boldsymbol{i}_1 = j\pi f_0 \boldsymbol{Z}^{-1}\boldsymbol{m}_{t_1}I_1/R_c; \quad \boldsymbol{i}_2 = j\pi f_0 \boldsymbol{Z}^{-1}\boldsymbol{m}_{t_2}I_2/R_c, \quad (37)$$

where $\boldsymbol{i}_k$ is a vector denoting the induced currents in receiving coils by the transmitting coil k, $k = 1, 2$; I_k is the excitation current of the transmitting coil k, $k = 1, 2$; the ith element in the vector $\boldsymbol{m}_{t_p}$ is the mutual inductance between transmitting coil TX_p and r_i, and $\boldsymbol{Z}^{-1}$ is the inverse of the impedance matrix, in which the diagonal elements are the coil resistance $2R_c$ and the off-diagonal element (p, q) is $j2\pi f_0 M_{r_p,r_q}$, where M_{r_p,r_q} is the mutual inductance between r_p and r_q. Considering the transmitting sources are independent, we can apply a signal combining vector $\boldsymbol{w}$ to maximize the SNR, which is

$$\arg\max_{\boldsymbol{w}} \frac{\boldsymbol{w}^H\boldsymbol{i}_1\boldsymbol{i}_1^H\boldsymbol{w}}{\boldsymbol{w}^H\boldsymbol{i}_2\boldsymbol{i}_2^H\boldsymbol{w}}, \quad s.t.\ \boldsymbol{w}^H\boldsymbol{w} = 1, \quad (38)$$

where H denotes hermitian, and we implicitly neglect the noise power since the communication channel is interference-limited as shown in preceding sections. The constraint is used to normalize the coefficient vector. The solution to (38) is the celebrated generalized Rayleigh quotient, i.e., $\boldsymbol{w}$ is the eigenvector associated with the largest eigenvalue of $(\boldsymbol{i}_2\boldsymbol{i}_2^H)^{-1}\boldsymbol{i}_1\boldsymbol{i}_1^H$. In this way, we can maximize the received power, while minimize the interference effect.

In Fig. 13, we consider a coil array with four elements and the inter-element interval is 0.02 m. The center of the coil array is aligned with the center of TX_1. All other configurations are the same as preceding sections. By applying the proposed approach, we can significantly reduce the interference effect. As shown in the figure, as TX_2 changes its position, the capacity of the channel between TX_1 and the receiver is almost a constant. The improvement comes from the diversity provided by the coil array. The vector $\boldsymbol{w}$ is designed to enhance the signals from TX_1 and minimize the signals from TX_2. As suggest in the figure, this algorithm works well when SNR is high, while when SNR is low its performance is not stable.

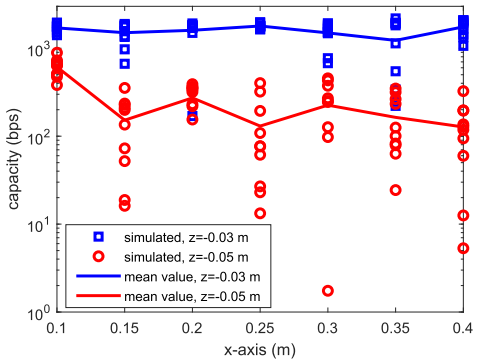

FIGURE 14. Capacity of the channel with interference and random coil array orientation. The curve is mean value and the circle and squares are simulated results. The red color is for $z = -0.05$ m and the blue color is for $z = -0.03$ m.

In addition, the coil array can reduce the random orientation effect. In Fig. 14, we consider a randomly orientated coil array, i.e., the orientation of the coil array is a random vector on the horizontal plane. Although in presence of the interference, the achieved capacity is several kbps with small variance as shown in the figure.

Although the proposed solution can achieve much better capacity, it requires the information of the wireless channel, i.e., mutual inductance. Thus, we need to conduct channel estimation before using the approach. Moreover, the accuracy of the channel estimation can significantly affect the performance.

V. CONCLUSION

Through-metal wireless communication using magnetic induction is a reliable and flexible solution for robots in metal-constrained environments. In this paper, we develop an analytical antenna-channel joint model to provide insightful understandings of the communication system. We find the optimal carrier frequency is at lower kHz band for 1 cm thick metal. More impressively, we provide a general equation to find the optimal frequency and coil configurations such as number of turns and radius, for metal walls with arbitrary thickness. In addition, we show that using a coil array, one can significantly improve the reliability of a communication system by reducing the orientation loss and avoiding mutual interference. This model can be leveraged to localize and track in-pipe robots in real-time. Also, we can analytically model the wireless connectivity of sensors/robots in metal-constrained environments to find an optimal deployment strategy. The model developed in this paper considers an infinitely large metal wall to obtain a simple solution to reveal the underlying physics of through-mteal wireless communication. Such a large metal wall is impossible to obtain in reality. In order to evaluate the communication performance of data transmission, we should consider a practical finite metal wall with boundaries or special metal structure such as cylindrical pipes. Our future work will consider the constraint of finite metal wall and conduct experimental evaluation of the communication system.

ACKNOWLEDGMENT

This article was presented at the 6th Annual IEEE International Conference on Wireless for Space and Extreme Environments (WISEE 2018), Huntsville, AL, USA, and was published in its Proceedings [1].

REFERENCES

[1] H. Guo, "Through-metal wireless communications with magnetic induction," in *Proc. 6th Annu. IEEE Int. Conf. Wireless Space Extreme Environ. (WISEE)*, Huntsville, AL, USA, Dec. 2018, pp. 42–47.
[2] H. Zangl, A. Fuchs, T. Bretterklieber, M. Moser, and G. Holler, "An investigation on wireless communication and power supply through metal tank walls," in *Proc. IEEE Instrum. Meas. Technol. Conf.*, May 2008, pp. 1452–1457.
[3] S.-G. Roh and H. R. Choi, "Differential-drive in-pipe robot for moving inside urban gas pipelines," *IEEE Trans. Robot.*, vol. 21, no. 1, p. 1–17, Feb. 2005.
[4] H. Schempf, E. Mutschler, V. Goltsberg, G. Skoptsov, A. Gavaert, and G. Vradis, "Explorer: Untethered real-time gas main assessment robot system," in *Proc. Int. Workshop Adv. Service Robot.*, vol. 3, 2003, pp. 1548–1558.
[5] D. Waleed, S. H. Mustafa, S. Mukhopadhyay, M. F. Abdel-Hafez, M. A. K. Jaradat, K. R. Dias, F. Arif, and J. I. Ahmed, "An in-pipe leak detection robot with a neural-network-based leak verification system," *IEEE Sensors J.*, vol. 19, no. 3, pp. 1153–1165, Feb. 2019.
[6] D.-X. Yang, Z. Hu, H. Zhao, H.-F. Hu, Y.-Z. Sun, and B.-J. Hou, "Through-metal-wall power delivery and data transmission for enclosed sensors: A review," *Sensors*, vol. 15, no. 12, pp. 31581–31605, Dec. 2015.
[7] T. J. Lawry, K. R. Wilt, J. D. Ashdown, H. A. Scarton, and G. J. Saulnier, "A high-performance ultrasonic system for the simultaneous transmission of data and power through solid metal barriers," *IEEE Trans. Ultrason., Ferroelectr., Freq. Control*, vol. 60, no. 1, pp. 194–203, Jan. 2013.
[8] J. D. Ashdown, L. Liu, G. J. Saulnier, and K. R. Wilt, "High-rate ultrasonic through-wall communications using MIMO-OFDM," *IEEE Trans. Commun.*, vol. 66, no. 8, pp. 3381–3393, Aug. 2018.
[9] W. Zhou, Y.-G. Su, L. Huang, X.-D. Qing, and A. P. Hu, "Wireless power transfer across a metal barrier by combined capacitive and inductive coupling," *IEEE Trans. Ind. Electron.*, vol. 66, no. 5, pp. 4031–4041, May 2019.
[10] H. Zangl, A. Fuchs, T. Bretterklieber, M. J. Moser, and G. Holler, "Wireless communication and power supply strategy for sensor applications within closed metal walls," *IEEE Trans. Instrum. Meas.*, vol. 59, no. 6, pp. 1686–1692, Jun. 2010.
[11] D. J. Graham, J. A. Neasham, and B. S. Sharif, "Investigation of methods for data communication and power delivery through metals," *IEEE Trans. Ind. Electron.*, vol. 58, no. 10, pp. 4972–4980, Oct. 2011.
[12] M. Yamakawa, Y. Mizuno, J. Ishida, K. Komurasaki, and H. Koizumi, "Wireless power transmission into a space enclosed by metal walls using magnetic resonance coupling," *Wireless Eng. Technol.*, vol. 5, no. 1, p. 19, Jan. 2014.
[13] C. Van Pham, A.-V. Pham, and C. S. Gardner, "Development of helical circular coils for wireless through-metal inductive power transfer," in *Proc. IEEE Wireless Power Transf. Conf. (WPTC)*, May 2017, pp. 1–3.
[14] H. Ishida, T. Kyoden, and H. Furukawa, "Super-low-frequency wireless power transfer with lightweight coils for passing through a stainless steel plate," *Rev. Sci. Instrum.*, vol. 89, no. 3, 2018, Art. no. 034706.
[15] J. H. Morecroft and A. Turner, "The shielding of electric and magnetic fields," *Proc. Inst. Radio Eng.*, vol. 13, no. 4, pp. 477–505, May 1925.
[16] G. Saulnier, H. Scarton, A. Gavens, D. Shoudy, T. Murphy, M. Wetzel, S. Bard, S. Roa-Prada, and P. Das, "Through-wall communication of low-rate digital data using ultrasound," in *Proc. Ultrason. Symp.*, Sep. 2006, pp. 1385–1389.
[17] R. Primerano, M. Kam, and K. Dandekar, "High bit rate ultrasonic communication through metal channels," in *Proc. 43rd Annu. Conf. Inf. Sci. Syst.*, Mar. 2009, pp. 902–906.
[18] H. Hu, Y. Hu, C. Chen, and J. Wang, "A system of two piezoelectric transducers and a storage circuit for wireless energy transmission through a thin metal wall," *IEEE Trans. Ultrason., Ferroelectr., Freq. Control*, vol. 55, no. 10, pp. 2312–2319, Oct. 2008.

[19] J. D. Ashdown, K. R. Wilt, T. J. Lawry, G. J. Saulnier, D. A. Shoudy, H. A. Scarton, and A. J. Gavens, "A full-duplex ultrasonic through-wall communication and power delivery system," *IEEE Trans. Ultrason., Ferroelectr., Freq. Control*, vol. 60, no. 3, pp. 587–595, Mar. 2013.
[20] R. H. Bhuiyan, M. R. Islam, J. M. Caicedo, and M. Ali, "A study of 13.5-MHz coupled-loop wireless power transfer under concrete and near metal," *IEEE Sensors J.*, vol. 18, no. 23, pp. 9848–9856, Dec. 2018.
[21] W. Cheng, "Thickness measurement of metal plates using swept-frequency eddy current testing and impedance normalization," *IEEE Sensors J.*, vol. 17, no. 14, pp. 4558–4569, Jul. 2017.
[22] O. Lucia, P. Maussion, E. J. Dede, and J. M. Burdìo, "Induction heating technology and its applications: Past developments, current technology, and future challenges," *IEEE Trans. Ind. Electron.*, vol. 61, no. 5, pp. 2509–2520, May 2014.
[23] W. Chew, *Waves Fields Inhomogeneous Media*. Piscataway, NJ, USA: IEEE Press, 1996.
[24] A. Vallecchi, S. Chu, L. Solymar, C. J. Stevens, and E. Shamonina, "Coupling between coils in the presence of conducting medium," *IET Microw., Antennas Propag.*, vol. 13, no. 1, pp. 55–62, Sep. 2018.
[25] H. Guo, Z. Sun, J. Sun, and N. M. Litchinitser, "M^2I: Channel modeling for metamaterial-enhanced magnetic induction communications," *IEEE Trans. Antennas Propag.*, vol. 63, no. 11, pp. 5072–5087, Nov. 2015.
[26] C. A. Balanis, *Advanced engineering electromagnetics*. Hoboken, NJ, USA: Wiley, 1999.
[27] C. Balanis, *Antenna Theory: Analysis and Design*. Hoboken, NJ, USA: Wiley, 2015.
[28] S. Kisseleff, I. F. Akyildiz, and W. H. Gerstacker, "Throughput of the magnetic induction based wireless underground sensor networks: Key optimization techniques," *IEEE Trans. Commun.*, vol. 62, no. 12, pp. 4426–4439, Dec. 2014.
[29] H. Guo, Z. Sun, and P. Wang, "Multiple frequency band channel modeling and analysis for magnetic induction communication in practical underwater environments," *IEEE Trans. Veh. Technol.*, vol. 66, no. 8, pp. 6619–6632, Aug. 2017.
[30] H. Guo and Z. Sun, "Increasing the capacity of magnetic induction communication using MIMO coil-array," in *Proc. IEEE Global Commun. Conf. (GLOBECOM)*, Dec. 2016, pp. 1–6.
[31] D. Wei, L. Yan, X. Li, J. Wang, J. Chen, M. Pan, and Y. R. Zheng, "Ferrite assisted geometry-conformal magnetic induction antenna and subsea communications for auvs," in *Proc. IEEE Global Commun. Conf.*, Dec. 2018, pp. 1–9.

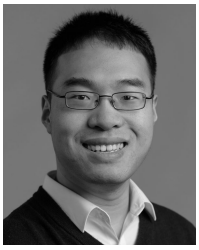

HONGZHI GUO (M'17) received the Ph.D. degree in electrical engineering from University at Buffalo, The State University of New York, Buffalo, NY, USA, in 2017. He was an Assistant Professor with the Engineering Department, University of Southern Maine, Portland, ME, USA. He is currently an Assistant Professor with the Engineering Department, Norfolk State University, Norfolk, VA, USA. He received the Best Demo Award at the IEEE International Conference on Computer Communications (INFOCOM), in 2017, and the Best Reviewer Award for the IEEE TRANSACTIONS ON WIRELESS COMMUNICATIONS, in 2017. He was a Research Scientist Intern with Genscape Inc., Louisville, KY, USA, in 2016,where he is involved in machine learning for automatic modulation detection. His current research interests include the Internet of Things in extreme environments, wireless power transfer, cyber-physical systems, and machine learning.

KYO D. SONG received the Ph.D. degree from the University of Nebraska–Lincoln, in 1992.

He is currently a Professor and the Chair with the Department of Engineering and the Center for Materials Research, Norfolk State University. He became an SPIE Fellow, in 2015. He has been working on several NASA projects, such as Hypersonic Flow Research, Testing High Temperature Materials for Scram-Jet Engine Components, Spectroscopic Analysis of Re-Entry Vehicle, Study on Effects of Atomic Oxygen on Space Materials, Wireless Power Transmission and Smart Materials Research for the Next-Generation Space Telescope (NGST), including development of neural probe using micro-spectrometer, and Surface Enhanced Raman Spectroscopy (SERS) under NASA supported grants. He has been involved in wireless power transmission (WPT) research area under various grants from NASA for more than 19 years. He has published more than 100 journal and conference papers and holds eight patents, including invention disclosure. He has also been serving as an Executive Committee Member and the Co-Chair of Nano-, Bio-, Info-Tech Sensors and Systems, and SPIE Conference for ten years.